Enhancement and underlying fatigue mechanisms of laser powder bed fusion additive-manufactured 316L stainless steel

Atef Hamada [a,*], Matias Jaskari [a], Tejas Gundgire [b], Antti Järvenpää [a]

[a] *Kerttu Saalasti Institute, Future Manufacturing Technologies (FMT), University of Oulu, Nivala, FI-85500, Finland*
[b] *Materials Science and Environmental Engineering, Tampere University, P.O 589, 33100, Tampere, Finland*

ARTICLE INFO

ABSTRACT

In this study, the enhancement of additively manufactured (AM) 316L, by annealing, to the fully reversed tension-compression fatigue performance, in terms of fatigue life and fatigue damage, were investigated under two conditions: as-built (AB) and heat-treated (HT) at 900 °C. The underlying fatigue mechanisms were comprehensively characterised through intensive microstructural observations of cyclic-strained microstructures and fracture surfaces using laser confocal scanning microscopy (LCSM) and secondary electron imaging using scanning electron microscopy (SEM). The experimental results showed that the fatigue resistance of HT 316L was significantly enhanced by 100% as the fatigue limit was increased from 75 to 150 MPa for AB and HT 316L, respectively. The fatigue cracking mechanism in AB 316L is mainly related to two imperfections of the AM-induced microstructural components: residual stresses, which cause highly localised deformation, and dendritic cellular structures, which possess a weak link in their grain boundaries against crack propagation. Upon heat treatment at 900 °C, the residual stresses and dendritic structure were effectively reduced. Consequently, the fatigue life of AM 316L was significantly enhanced by promoting the formation of high-angle boundaries. More precisely, the cyclic deformation processes in fatigued HT 316L involve persistent slip bands and strain hardening.

1. Introduction

Additive manufacturing (AM) technology has promoted new industrial concepts by revolutionising many sectors relevant to the aerospace, medical, automotive, and general manufacturing industries, making them faster and more cost-effective. This modern technology can manufacture complex designs that were difficult or expensive to manufacture previously with traditional manufacturing methods [1–3]. Furthermore, AM materials are compatible with those manufactured conventionally in terms of quasi-static mechanical properties, considering the significant differences in grain structure [4,5].

However, a major concern for metallic materials fabricated by AM in service is the fatigue performance property, and this is the key to using materials in structural applications subjected to cyclic loading, which causes a common mode of mechanical failure in many engineering structures [6].

Enhancing the fatigue properties of 3D-printed metallic structures, such as aluminium alloys [7,8], Ni-based alloys [9,10], maraging steels [11,12], and 316L [13,14], is a major challenge when utilising printed

parts in structural applications subjected to cyclic loading. The microstructural details of AM products, such as defect type, morphology, size, and surface roughness, can significantly affect the fatigue strength.

It has been well reported that the AM processing parameters can significantly affect the microstructure and internal and surface defects, which consequently affect the mechanical properties [15]. 316L stainless steel is a common, major alloy used in various industrial applications, such as in medical, chemical, marine, and aerospace industries and in nuclear power stations [16]. This is because of their thermal stability, high corrosion resistance, and good mechanical properties at room and cryogenic temperatures. As reported in a recent review article by Ahmed et al. [17], several authors have focused on improving the mechanical properties of AM 316L by optimising the process parameters, such as the laser power, scanning speed, hatch spacing, layer thickness, and scanning patterns, to achieve the highest build density. Jaskari et al. [18] studied the effect of the volume energy density of AM 316L on the microstructure and mechanical properties of defects. They reported no influence of energy density on the yield and tensile strengths; however, the elongation increased with increasing printing

* Corresponding author.
E-mail address: atef.hamadasaleh@oulu.fi (A. Hamada).

energy.

Another approach was applied to increase the mechanical strength of AM 316L by incorporating reinforcements, such as SiC and TiC particles, into 316L stainless-steel powder using low-energy ball milling [19,20]. In the same context, Zhai et al. [21–23] achieved grain refinement of AM 316L by adding TiC particles. Consequently, the yield and tensile strengths were remarkably enhanced without sacrificing elongation. These strengthening approaches enhanced the fatigue property of AM 316L.

The design of AM components for carrying dynamic loading is still in its infancy because the fatigue resistance and correlated deformation mechanisms of AM metallic materials under cyclic loading are not yet fully understood. Recently, Becker et al. [24] published a review article on the high-cycle fatigue strength (HCFS) of AM 316L, fabricated by laser-powder bed fusion (L–PBF) under as-built (AB) and post-processing conditions. The articles surveyed in that review reported a low fatigue resistance of AB 316L with an HCFS of 90 MPa. Roirand et al. [25] studied the effects of various laser scan patterns on the defect density, microstructure, and fatigue resistance of AM 316L. They found that a meandering laser pattern without rotation between the layers promoted a printed microstructure with a very low porosity density. Consequently, the fatigue resistance increased significantly. Pelegatti et al. [26] studied the critical factors influencing the low cycle fatigue (LCF) of L–PBF 316L. They emphasised that premature crack nucleation emerged from voids near the surface. In addition, defects arising from lack-of-fusion defects that were 400 μm are more detrimental to reducing the fatigue life than semi-spherical pores. Kluczyński et al. [27] studied the effect of process parameters and the correlated printing energy density on the LCF behaviour of 316L. They found that the cyclic deformation energy stored in the cyclically strained structure, represented by hysteresis loops, was significantly influenced by the features of the achieved microstructures at different process parameters. Liang et al. [28] conducted a series of HCF tests on AB and hand-polished AM 316L under different loading modes, namely, tension, bending, and torsion fatigue. They found that the fatigue performance of AM 316L decreased because of inherent surface defects. Hatami et al. [29] studied the effect of post-machining on the high-cycle fatigue of AB 316L at a stress ratio of R = 0.1. They reported that post-machined 316L specimens exhibited higher fatigue strengths than AB 316L owing to the presence of pores and surface defects. Pegues et al. [30] studied the mechanical properties and fatigue performance of LB–PBF 304L SS after machining and electro-polishing. They found that LB–PBF 304L with its unique microstructural features promotes a higher fatigue resistance than its wrought counterpart by avoiding the typical fatigue cracking initiation mechanisms, that is annealing twin boundaries (Σ3-TB) and high-angle grain boundaries (HAGB). Recently, Rautio et al. [31] applied a surface modification technique called shoot peening (SP) to study the fatigue resistance of L–PBF 316L. A pronounced improvement in the fatigue resistance of shoot-peened AM 316L was also reported. The fatigue limit tripled from 200 MPa for non-SP to 600 MPa for SP AM 316L. A recent review by Malakizadi et al. [32] reported the effects of post-processing operations on the mechanical performance, tensile strength, hardness, and fatigue properties of 316L, Ti6Al4V, and Alloy 718. Studies have suggested that surface-finish treatments can notably improve the fatigue strength of metallic AM materials. However, they concluded that the optimal selection of AM process parameters to minimise the density of LBPF-induced microstructural defects (e.g. porosity and lack of fusion) has a greater influence than subsequent post-processing. Hence, the fatigue performance of AM parts should be improved by preventing the formation of microstructural defects during AM printing.

The underlying damage mechanism during the cyclic loading of AM 316L has not yet been completely understood. Furthermore, most prior work on the fatigue behaviour of AM 316L was carried out to correlate the printing parameters with microstructural imperfections and fatigue life. The aim of this study was to enhance the fatigue resistance of AM 316L by identifying the underlying fatigue damage mechanisms and investigating the influence of a short annealing time at 900 °C on the microstructure and fatigue resistance. This was studied by conducting force-controlled fatigue experiments and a comprehensive microstructure analysis of AB/heat-treated (HT) 316L specimens that underwent cyclic plastic deformation.

2. Experimental methods

The experimental 316L powder employed for printing via LB–PBF was supplied by Electro Optical Systems Oy (EOS). The powder has been sieved to prevent large powder on the order of 50 μm. The chemical compositions of the 316L powder used in the 3D printing and the counterparts of the as-built material are listed in Table 1. The studied materials were printed by an EOS machine (Model:290 M) at EOS Electro Optical Systems Oy (Finland).

According to the standard ASTM E8M, round fatigue specimens with a total length of 55 mm and a diameter of 6 mm were vertically printed with certain laser-processing parameters to induce a volume energy density of 40 J/mm^3. Fig. 1 shows the geometry of the 3D-printed fatigue test sample and building direction (BD). Another series of fatigue specimens underwent heat treatment at 900 °C for 30 min in a muffle furnace (ether) under an argon atmosphere. The heat-treated material was denoted as HT 316L.

Residual stress (RS) measurements were performed using an Xstress 3000 X-ray diffractometer (Stresstech Oy, Finland). Measurements were taken at both the surface and central regions. To measure RS at the depth of the central region, electropolishing using a Struers MoviPOL 5 electropolisher in a perchloric acid solution was applied to remove the material layers up to the central region.

High-cycle fatigue tests were conducted at room temperature in a symmetrical push–pull cycle using a Zwich electromagnetic resonator fatigue machine (Vibrophore – resonance testing system) with a maximum load of 50 kN under a force control mode. The fatigue tests were conducted at a frequency of 100 Hz with zero mean stress. The fatigue damage mechanism was extensively studied by examining the cyclic strained microstructures using a laser confocal scanning microscope (LCSM, KEYENCE/VK-X200). The fracture surfaces of the failed specimens, AB and HT 316L, were examined using secondary electron imaging with a field-emission gun scanning electron microscope (FEG–SEM; Carl Zeiss Ultra Plus). The microindentation hardness was measured using a microindentation tester (CSM Instruments). A diamond Berkovich indenter with a three-sided pyramid was used to conduct a series of indentations with a maximum indentation load of 2 N.

3. Results

The surface features of AB 316L, such as morphology, topographical cues, and imperfections, were depicted using SE imaging. As shown in Fig. 2(a), powder particles adhered to the outer surface, and partially melted particles were clearly observed. These surface particles are undesired in AM products because they are expected to increase the surface roughness owing to balling [33]. In the magnified view in Fig. 2(b), the surface is free from detrimental defects. such as large pores, keyholing,

Table 1

Composition of the supplied 316L powder used for L-PBF manufacturing of 316L and the corresponding composition of the as-built (AB) material.

Element, wt. %	C	Mn	Cr	Ni	Mo	Cu	Si
powder	0.03	2	17*/ 19**	13*/ 15**	2.2*/ 3**	0.5	0.75
AB	0.018	1.42	17.9	12.8	3	0.24	0.34

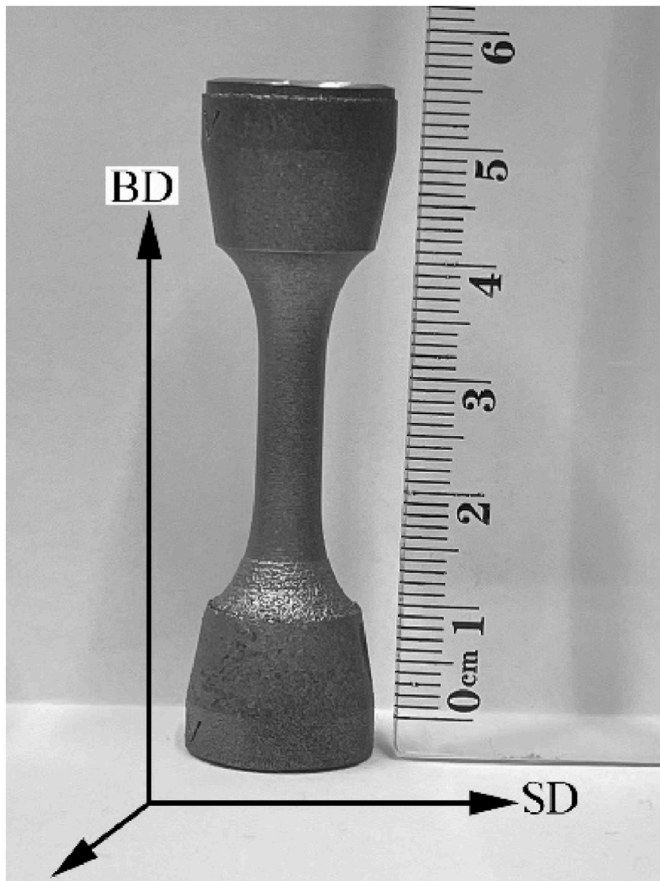*, ** symbols show the minimum and maximum contents of the element.

Fig. 1. Macrograph of the fatigue test of the 316L samples printed by the L-PBF technique showing the geometry and building direction.

and microcracks. It has been reported that undesired surface defects during the LPBF printing of metallic materials are induced by improper printing parameters [34–36]. Thus, the adapted printing parameters and consequent energy density resulted in a high surface quality without defects on the 316L material under consideration.

The microstructural characteristics of AB and HT 316L were observed using LC-SM, as shown in Fig. 3. A "fish scale morphology" with melt pool boundaries is clearly shown in Fig. 3(a). This fish-scale morphology arose from the melting tracks generated by the laser beam [37]. The magnified view of a single pool shows columnar grains and an elongated submicron cellular substructure; see Fig. 3(b)). These characteristics are consistent with the microstructure reported for 316L printed using LPBF [38–42]. It is well established that the cellular substructure promoted by fast solidification during the 3D printing of 316L has high-density dislocation network cell boundaries and elemental

segregation, as reported by Sun et al. [43].

The effect of the HT at 900 °C on the microstructure of AB 316L is displayed in Fig. 3(c and d).

A striking feature of the HT 316L structure was the appearance of high-angle boundaries inside the initial pools, as shown in Fig. 3(c). A recrystallised grain structure with a significant dissolution and breakdown of the cellular substructure is promoted with HT at 900 °C. In agreement, Edin et al. [42] found that the initial annealing temperature to dissolute and break the cellular substructure of the AB 316L is 800 °C. At a higher temperature of 900 °C and with a long annealing time, the cellular substructure is effectively eliminated. The fish-scale morphology and strip-shaped melt tracks, highlighted by arrows, can be clearly observed. These tracks illustrate the laser beam melting paths via "track-by-track" and "layer-by-layer" manufacturing, as reported by Zhao et al. [44].

Furthermore, a small fraction of the dendritic cellular substructure, highlighted by the yellow circles, was still present even after HT at 900°C for 30 min; see Fig. 3(c). Interestingly, the fine residual cellular substructure remaining after annealing 316L was explored by extracting the 3-dimensional (3D) profile image of the HT microstructure in Fig. 3 (c). As shown in Fig. 3(d), irregular small red zones are present between the pools. These zones are the counterparts of the residual cellular dendritic substructure highlighted by the circles in Fig. 3(c). The use of this technique (3-D imaging by LCSM) to determine the zones of the dendritic cellular substructure in the AM and annealed structures of 316L at various temperatures will be discussed separately in another manuscript.

The microindentation hardness (H_{IT}) values of AB and those for HT 316L were evaluated using a Berkovich indenter equipped with an instrumented microindentation tester (CSM Instruments). Fig. 4 shows the load–penetration depth (P-h) and loading–unloading curves extracted from the microindentation tests. The HT 316L, shown by the red curve, shows a higher penetration depth, i.e. a lower hardness H_{IT}, than that of AB 316L. The measured H_{IT} values of the AB and HT 316L are 2690 ± 166 and 2295 ± 82 MPa, respectively. This drop in hardness upon annealing is attributed to losing the strengthening parameter of the cell boundaries, which comprise high-density dislocations [40,45].

The high-cycle fatigue (HCF) behaviour over up to 10^7 cycles was experimentally assessed by high-efficiency electromagnetic resonance fatigue testing of the studied material. Fig. 5 shows the experimental data from the fatigue tests, that is, the stress amplitude vs. the number of cycles to failure (S–N) plots of structures AB and HT 316L. A significant improvement in the fatigue resistance was found for HT 316L because the fatigue limit (σ_{FL}) of L-PBF 316L is relatively small at ~75 MPa. After the heat treatment at 900°C, the σ_{FL} of HT 316L increased to ~150 MPa. Dastgerdi et al. [46] reported S–N plots of AM 316L fabricated by L-PBF in vertical and horizontal building directions for layer thicknesses of 20 μm and 40 μm. They found that the build orientation and layer thickness had a significant impact on the fatigue resistance. Meanwhile, the AB 316L material did not achieve the fatigue limit (i.e. the stress amplitude at which no failure occurred after 10^7 cycles). They correlated the short
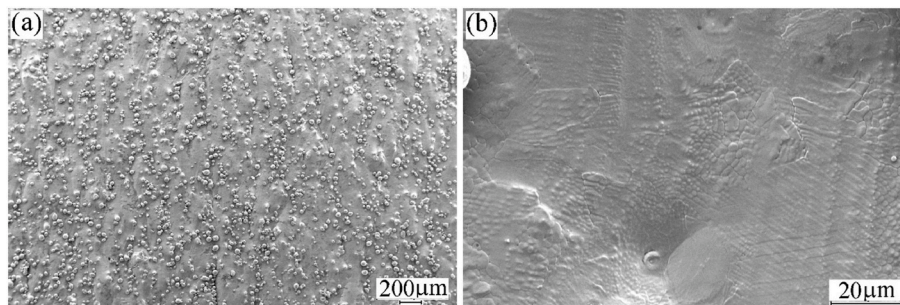

Fig. 2. SEM micrographs of the outer surface of the 3D-printed 316L by the L-PBF technique: a) the outer surface particles, and (b) a magnified view of (a) the defect-free surface.
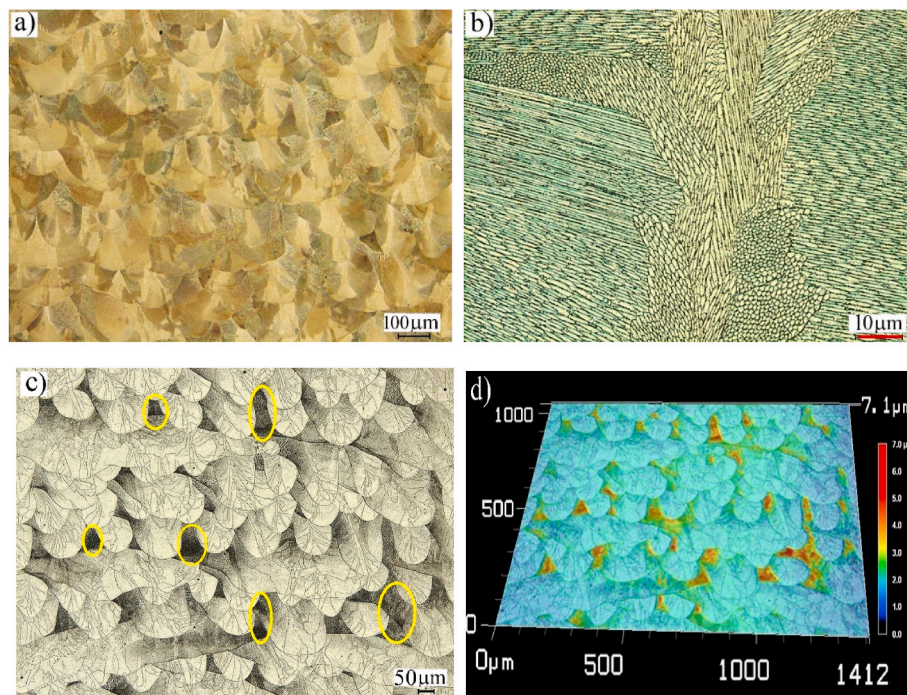
Fig. 3. Microstructure of the L-PBF 316L as captured by LCSM: (a) as-built structure, (b) high magnification of (a) displaying the cellular/columnar substructure nature of the grain structure, (c) heat-treated microstructure of AM 316L at 900 °C for 30 min, and (d) 3D profile image of (c).
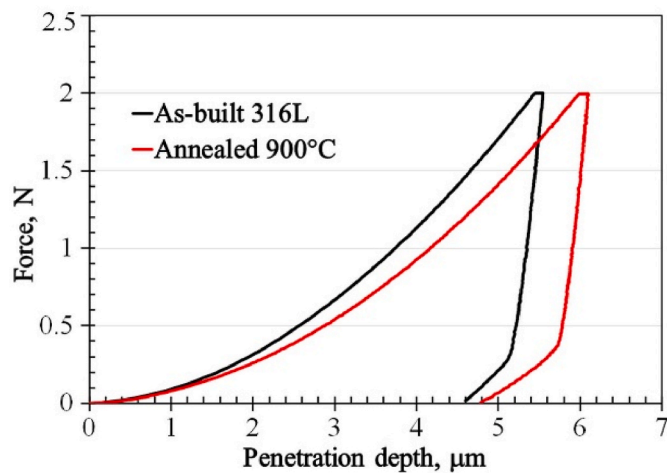

Fig. 4. Load–penetration depth (P-h) curves from microindentation hardness tests conducted on the as-built (black curve) and annealed 316L (red curve). (For interpretation of the references to colour in this figure legend, the reader is referred to the Web version of this article.)

Fig. 5. Stress amplitude–fatigue life data (S–N curves) of the high-cycle fatigued AM 316L with the as-built and heat-treated structures.

fatigue life of AB 316L with the internal and surface defects. Similarly, Wang et al. [47] compared the fatigue performance of AM 316L to that of its wrought counterpart. They found that the SLM-316L had a lower σ_{FL} than that of the wrought material, at 90 and 166.5 MPa, respectively. Ponticelli et al. [48] studied the reverse bending fatigue response of 316L printed using LPBF for various building orientations (0°, 45°, and 90°) and volumetric energy densities. Overall, they found that the σ_{FL} of various sets of AM 316L was as low as 20% of the ultimate tensile strength, while the σ_{FL} of the counterpart bulk 316L was 50% of its ultimate tensile strength.

To investigate the fatigue crack initiation and propagation in the studied material, specimens that fatigued up to failure were longitudinally sectioned and subjected to gentle grinding and polishing. Fig. 6 shows the deformed AB microstructure under cyclic loading at 200 MPa.
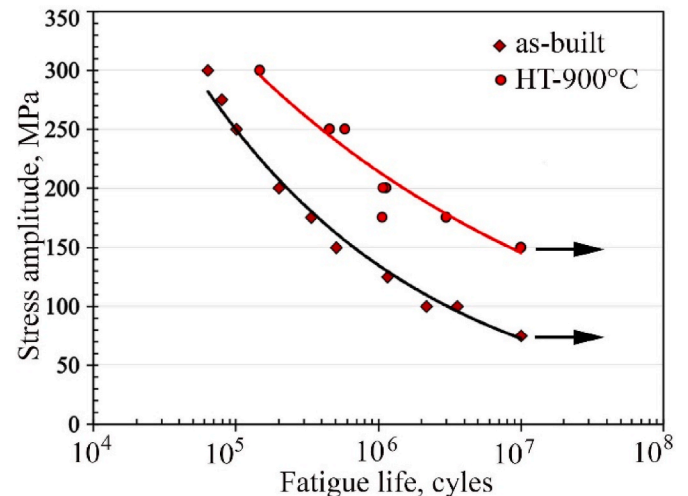
As shown in Fig. 6(a), two main cracks were observed in different zones. Crack I emerged from the surface and propagated internally. Crack II emerged from the inner layer and predominantly propagated transgranularly. Interestingly, the round pores inside the microstructure, indicated by the arrows, did not show a related crack. The corresponding 3D image in Fig. 6(b) shows that crack I initiated at a powder particle located on the surface. Subsequently, the cracks extended the internal microstructure along the direction perpendicular to the loading. Similarly, on the right side of the cross section of the sample in Fig. 6(c) illustrates several fatigue cracks in the cyclic strained AB structure at 200 MPa. Whereas crack I emerged from the surface, cracks I and III emerged from the inner surface. The magnified view shows that crack II was internally initiated at a defect located at the melt-pool boundary, as indicated by the white arrow in Fig. 6(d). In addition, two round pores were observed in the cellular substructure, as highlighted by the dashed
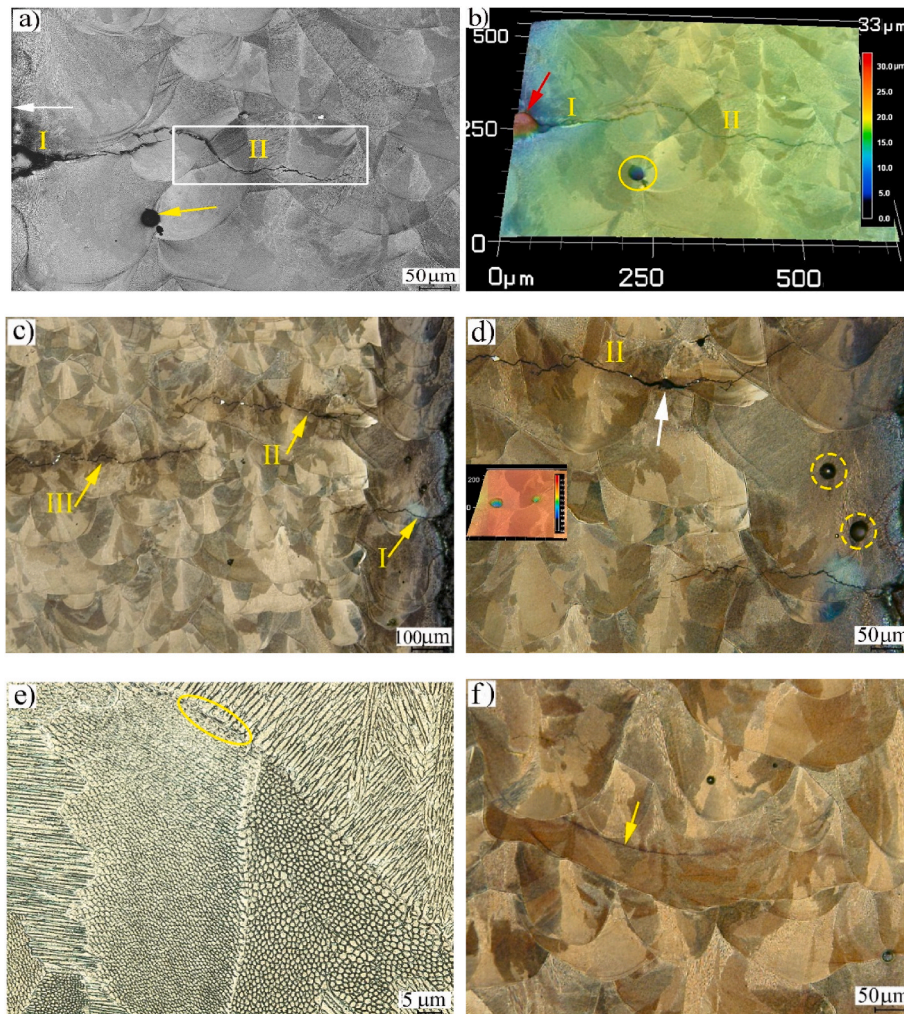
Fig. 6. Laser confocal scanning microscope images of fatigue cracking evolution of the as-built 316L at a stress amplitude of 200 MPa: (a) fatigue cracks 1 and II (b) 3D profile of (a), (c) various fatigue cracks, (d) a magnified view of (c), (e) fatigue crack embryos, and (f) microcracks at the pool boundary.

circles. There is no evidence of emerging fatigue cracks in these pores.

It is now well established that the failure of additively manufactured metallic materials is attributed to a common cause: the presence of microstructure defects (pores, lack of fusion, unmelted powder) [49–54]. These defects caused local discontinuities in the microstructure; consequently, the stress concentration at these defects caused local plastic deformation. In this approach, the cyclic deformation of the defective microstructure in AM 316L leads to the formation of microcracks at these defects. In a recent study, Tomaszewski [55] estimated the fatigue behaviour of L-PBF 316L based on a defect size effect model. They found that the defect size did not significantly affect the fatigue strength of AM 316L.

At a high magnification, fatigue-cracking embryos were observed on a pool boundary in the AB structure, as shown in Fig. 6(e). Hence, fatigue microcracks were generated at the pool boundaries, as shown in Fig. 6(f).

The characteristic features of the fracture surface of the cyclically strained AB 316L were examined using SEM to describe the underlying fatigue deterioration process of the AB structure in AM 316L. It is well established that fatigue crack initiation and propagation in a material are substantially influenced by the microstructure, grain and phase structure, and strength of the matrix [56]. However, fatigue studies of AM materials have mainly correlated the fatigue damage of metallic materials additively manufactured with internal defects, large pores, lack-of-fusion [57,58], and surface roughness [6,59,60]. Fig. 7 shows

distinct regions on the fracture surface of AB 316L cyclically strained at a stress amplitude of 150 MPa. A crack initiation zone located at the surface edge of the fatigued specimen is shown in the SEM image in Fig. 7(a).

Surface particles, labelled (P), adhered to the outer surface, and another partially melted particle was located directly under the surface, which is highlighted by the yellow square. A magnified view of the particles highlighted particle in (a) is shown in Fig. 7(b). Interestingly, a fatigue crack was initiated in the particles located under the surface. This was attributed to the localised strain at the defect site [61]. Another crack initiation region without defects was observed at the surface, as shown in Fig. 7(c). Crack initiation sites were arranged by identifying traces of persistent fatigue slip bands (PSB). It is well established that PSBs comprise extrusions–intrusions, that is, a tongue-like topography [62]. At a high magnification, intrusion roots and protrusions of PSBs were observed at the crack initiation site, as shown in Fig. 7(d). During the cyclic straining of FCC structural materials, such as steel 316L, these localised strain bands (PSBs) are preferentially formed from favourably oriented slip planes. Consequently, extrusions and intrusions on the specimen surface promoted a dislocation pile-up that impinged on the structural boundaries. Hence, fatigue cracks nucleate because of the local high cyclic plastic strain in PSBs [63,64]. In Fig. 7(e), crack tortuosity along the melt-pool boundary is observed, as indicated by the arrow. Simultaneously, an array of elongated layers is shown, as highlighted by the yellow oval. This is attributed to crack propagation along
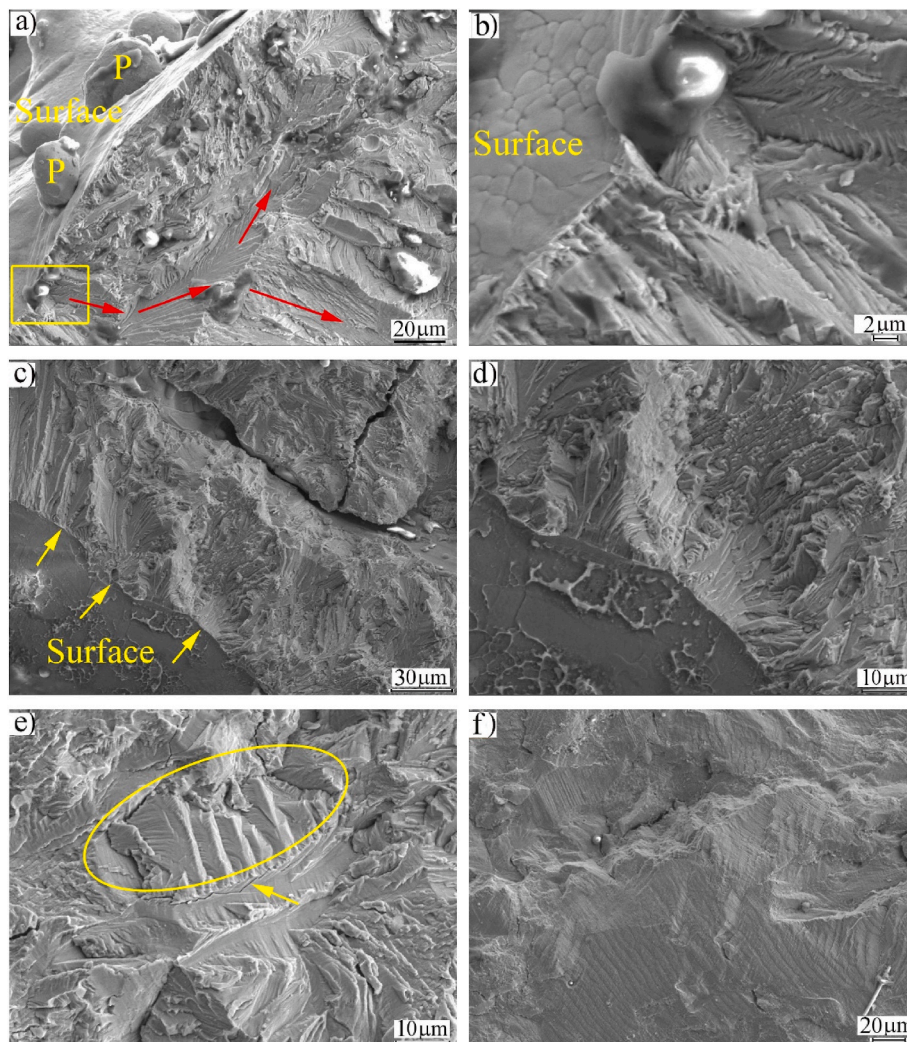
Fig. 7. SEM images of the fracture surface of the fatigued as-built 316L at the stress amplitude of 150 MPa: (a) a general view of a crack initiation site related to unfused surface particles, (b) a magnified view of (a), (c) a general view of the crack initiation site related to interactions of persistent slip bands (PSBs) with surface boundaries, (e) microcrack along the pool boundary, and (f) the crack propagation zone.

the intercellular boundaries. Notably, the fatigue cracking in AB 316L propagated in a ductile manner because regular fatigue striations were observed on the fracture surface, as shown in Fig. 7(f). Thus, a high degree of plasticity was involved in the cyclic deformation of AM 316L.

The microstructure of the HT 316L fatigued at 200 MPa until failure, as shown in Fig. 8. One striking feature is the presence of multiple gas pores at locations adjacent to the pool boundaries, as shown in Fig. 8(a). The corresponding 3D image of the pores is shown in Fig. 8(b). The pore depths were estimated by analysing the topography of the features in the 3D image. The pores had a depth of 15 m, and the total area of the pores was estimated relative to the matrix area in the LCSM images. The average pore area fraction was 0.008 per unit μm^2. This indicates that the area of the sound matrix without pores was 0.992. This is in agreement with the measured mass density of 3D-printed 316L using the Archimedes method, which estimated that the relative density of 3D-printed 316L was 99.6. The 3D image did not show fatigue microcracks in these pores. Riemer et al. [65] found that the pores in AB 3016 L had an insignificant effect on the fatigue properties and crack growth behaviour during cyclic loading at high-cycle fatigue. In another region of the microstructure, however, two cracks (I, II) formed at the printing defects, as highlighted by dashed red ovals in Fig. 8(c). A magnified view of crack I is shown in Fig. 8(d). The oxide defects broke during cyclic deformation. Consequently, fatigue cracking was promoted along the

grain boundaries where the oxide was located.

The corresponding 3D profile of the cracked oxide defects in Fig. 8(d) are shown in Fig. 8(e). The oxide defect was fragmented irregularly into two parts, and the cracks propagated in multiple directions. Hence, the crack causes a void depth of 10 μm. This reveals the distinct nature of the fatigue cracking of AM materials from that of their counterpart bulk materials. Interestingly, multiple microcracks were observed at the boundaries of the residing dendritic cellular regions, as highlighted by yellow circles in Fig. 8(f).

The fatigued fracture surfaces of the HT 316L specimens are shown in Fig. 9. The crack initiation zone is shown in Fig. 9(a). A striking feature of the crack initiation zone is the disappearance of pores and other imperfections that induce fatigue initiation in the AM metallic materials. Fatigue slip markings were clearly observed in this zone. A magnified view of (a) is shown in Fig. 9(b). Clear evidence of a microcrack at the surface boundary is highlighted by the dashed yellow circle. This was a result of the interactions of persistent slip bands (PSBs) in grain (I) with the boundaries. However, tiny voids are observed in grain II. Fig. 9(c) shows a high-magnification image of these tiny voids in grain II. These tiny voids, highlighted by red dashed circles, occur at the interfaces between the residual cellular grains and the recrystallised grains. Hence, these tiny voids represent fatigue crack embryos. Hence, fatigue microcracks are promoted at these boundaries, as shown in Fig. 8
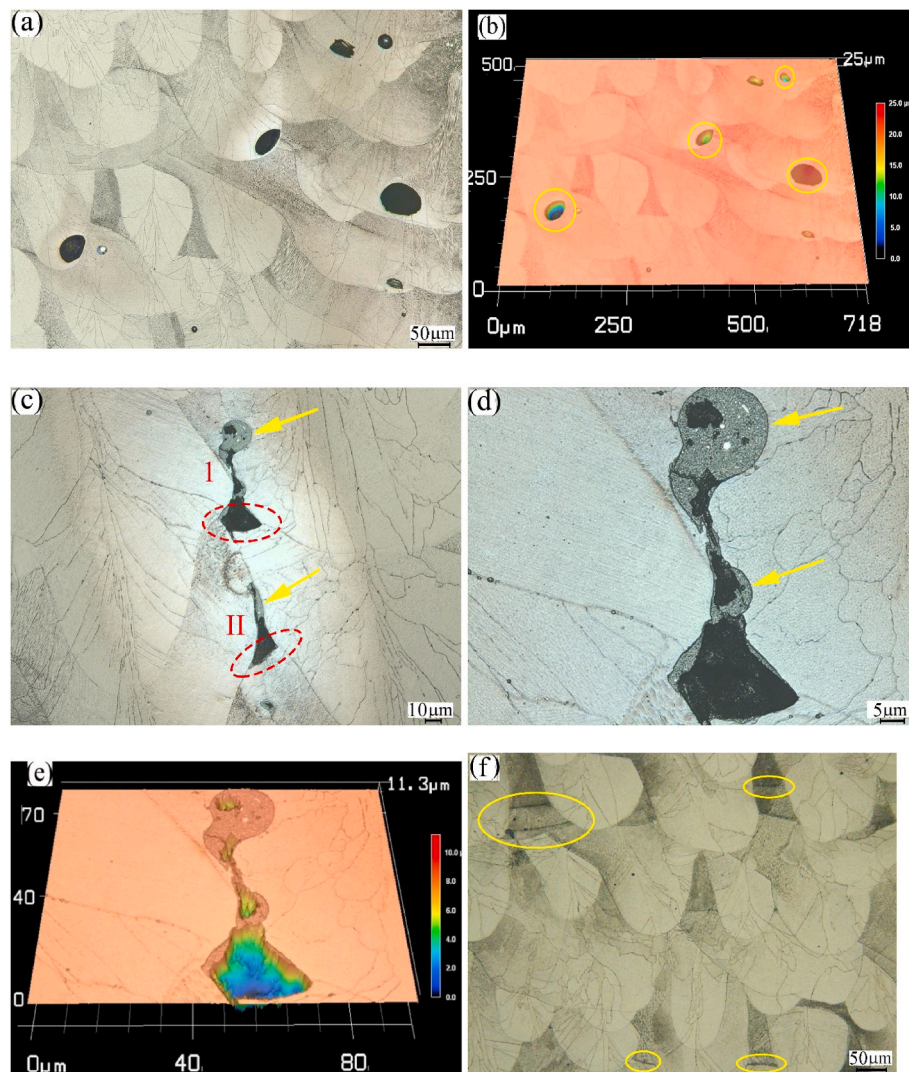
Fig. 8. Laser confocal scanning microscope images of the fatigue cracking evolution of the heat-treated 316L at the stress amplitude of 200 MPa: (a) pores in the HT 316L fatigued at 200 MPa, (b) 3D profile of (a), (c) cracks related to oxide defects, (d) a magnified view of (c), (e) 3D profile of (d), and (f) multi microcracks located at the boundaries of rest dendritic regions.

(f). The crack initiation region is shown in Fig. 9(d). Similarly, intensively clustered fatigue slip bands without imperfections were observed on the fracture surface. This emphasises that HT 316L underwent cyclic plastic deformation by inducing intensive fatigue slip bands. Subsequently, PSBs intersect with the grain boundaries, as in fatigued polycrystalline fcc metals, to form fatigue crack embryos and microcracks [62,66].

4. Discussion

Here, we will discuss the main cause for enhancing the fatigue resistance of AM 316L by annealing at 900 °C and the underlying fatigue damage mechanisms in both materials, AB and HT 316L.

The S–N plots shown in Fig. 5 displayed a significantly higher fatigue resistance of the HT structure than that of AB 316L. This is mainly attributed to the microstructure promoted by HT. Based on observations of the HT microstructure, the main causes/defects, that is, pores and lack of fusion, for fatigue failure in AM 316L are present and were not omitted upon annealing treatment, as shown in Fig. 8.

It is well known that residual stresses are induced in the as-built structures of metallic materials additively manufactured by the L-PBF technique owing to steep spatial and high thermal gradients [67]. Wu

et al. [68] investigated AM-induced residual stress (IRSs) in 316L. They found that the AM-IRS is the compressive type near the AB centre and tensile type near the surface. Furthermore, the IRSs caused significant localised deformation in the vertically built samples. This implies that defects located at the surface are subjected to tensile RSs, which can induce crack initiation and propagation. Consequently, these defects are favourable sites for fatigue cracking owing to the localised deformation and plasticity-induced crack opening. Bian et al. [69] studied the effect of laser power and scanning strategy on the RS distribution in AM-316L. They found that by increasing the laser power from 160 W to 200 W, the tensile RS increased. In the present study, the average RS was measured in the AB and HT 316L samples at different locations, for example at the surface and near the central region. Fig. 10 shows pronounced RSs at both the surface and centre of the AB structure. For instance, the RSs values in the AB state were 311 and 303 MPa in the areas near the surface and centre, respectively. These tensile-type RSs have a detrimental effect on fatigue behaviour, as faster fatigue cracking initiates in AB 316L compared to that in its HT counterparts. However, the applied HT at 900 °C was effective to reduce the RSs by 82 and 90% at the surface and centre, respectively. In the same context, Shiom et al. [70] found that stress-relieving annealing at 600 and 700 °C for 1 h was effective to reduce the RSs by ~70%.
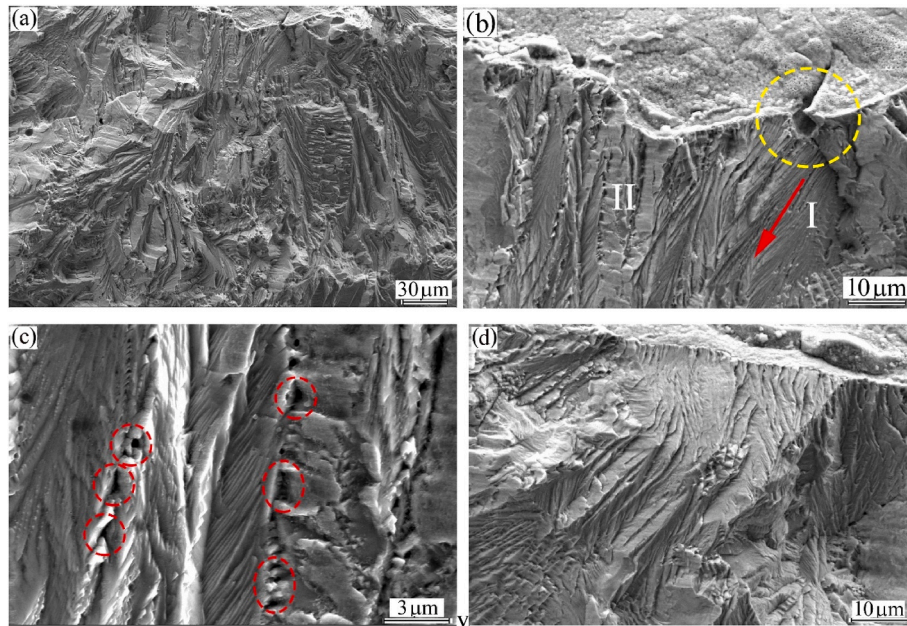
Fig. 9. SEM images of the fracture surface of the fatigued HT 316L at the stress amplitude of 175 MPa: (a) general view of a crack initiation site, (b) magnified view of (a), (c) general view of Zone II in (b), and (d) persistent slip bands (PSBs) on the fracture surface.
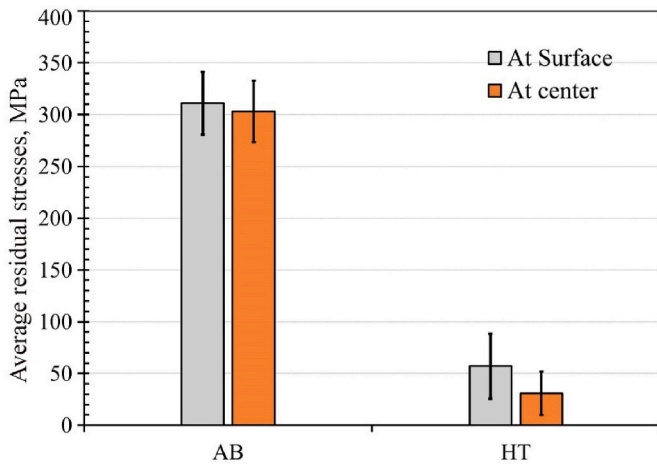

Fig. 10. Effect of heat treatment on the induced residual stresses in AM 316L.

Besides the detrimental effect of IRSs on the fatigue resistance, the dendritic cellular structure in AB has a significant effect on the fatigue properties. Fig. 11 shows the fatigued microstructure of AB 316L at 250 MPa. A gas pore size of 12 μm was observed on the pool boundaries

without microcracking into the structure, as shown in Fig. 11(a). The gas pores that appear in the fatigued microstructures (Figs. 6 and 8) are assumed to be under the critical size to result in premature fatigue failure. It is well established that gas pore defects smaller than the critical size have no detrimental effects during cyclic plastic deformation. Thus, the fatigue resistance depends on the damage behaviour of the microstructure in proportion to the hardness [55]. Furthermore, the impact of the dendritic cellular structure in the AB state on fatigue crack propagation becomes significant. This is because the crack propagation is faster through the cell interfaces, as shown in Fig. 11(b). This is attributed to the low resistance of the fatigued AB dendritic structure to crack propagation. The cyclic strain hardening/softening behaviours of fatigued AB and HT 316L at a constant stress amplitude were measured by microindentation hardness (H_{IT}).

Fig. 12 shows that the fatigued HT 316L, which was softer than its counterpart AB 316L before fatigue (see Fig. 4), exhibited a higher hardness after fatigue, that is, the HT microstructure underwent cyclic hardening. However, AB 316L exhibited cyclic softening because its hardness was relatively reduced by cyclic straining.

The cyclic hardening/softening ratio was quantified based on the difference in hardness before and after fatigue testing. The HT 316L exhibited a cyclic hardening ratio of ~18%, whereas the AB 316L displayed a cyclic softening ratio of 22%.

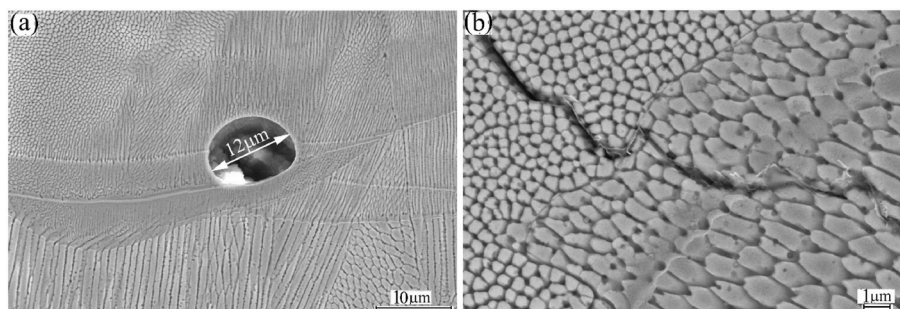During the progressive cyclic straining of HT 316L, dislocation

Fig. 11. SEM microstructures of the fatigued AB 316L at a stress amplitude of 250 MPa: (a) a small pore located on the pool boundaries and (b) fatigue crack propagation along the cellular grain interfaces.
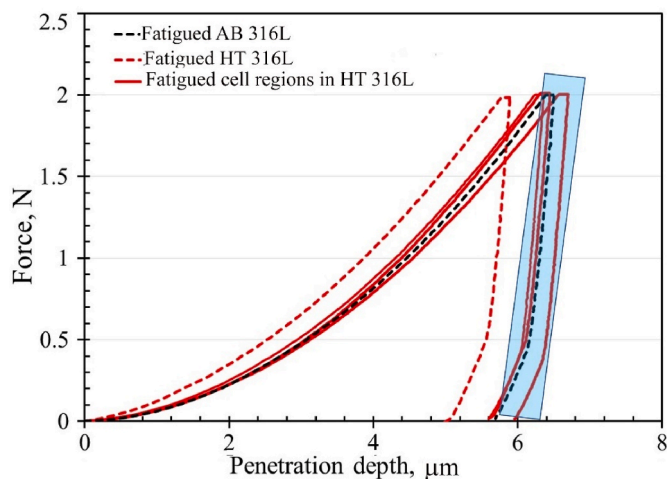
Fig. 12. Load–penetration depth (P-h) curves from microindentation hardness tests conducted on the as-built (dashed black curve) and HT 316L (dashed red curve) after cyclic plastic deformation. (For interpretation of the references to colour in this figure legend, the reader is referred to the Web version of this article.)

accumulation and the interaction of dislocation mechanisms are assumed to be induced in the matrix during fatigue deformation. Consequently, the strain hardening of the HT is promoted. Interestingly, we measured the hardness of the three residual cellular substructure regions in HT 316L to compare their cyclic response with that of their counterpart AB dendritic structure. It is apparent from the hardness measurements that the residual cellular substructure regions underwent cyclic softening, similar to the AB structure, as highlighted by the blue shadow in Fig. 12. Thus, cyclic plastic deformation is highly accommodated at the boundaries of the cellular substructure owing to dislocation dynamics during fatigue. Consequently, fatigue microcracking associated with cellular boundary deformation is promoted.

Based on our results, we should refer to a striking characteristic of the AM metallic 316L in terms of fatigue strength to tensile strength ratio (σ_{FL}/σ_{UTS}). It is reported that for conventional and wrought steels, this ratio σ_{FL}/σ_{UTS} is in the range of 0.4 to 0.6 [71,72]. The estimated ratios of the studied AB and HT 316L are 0.12 and 0.24, respectively. These values are not within the well-reported range of the fatigue strength/tensile strength ratios for wrought steels. The cyclic straining capacity and average resistance to cyclic plastic deformation of a metallic structure determine its fatigue limit. However, changing microstructural features, such as grain structure, defects, and residual stresses, by a new metallurgical process significantly contributes to the fatigue damage mechanism. AM technology is significantly different for fabricating metallic structures in 3D with various microstructural characteristics. Hence, the rule of the σ_{FL}/σ_{UTS} ratio of fatigue resistance for wrought steels could not be applied on metallic steels fabricated by AM. The LBPF-induced microstructural defects (pores, dendritic cellular structure, and residual stresses) induce a cyclic damage mechanism and markedly affect the fatigue limit. However, wrought steels undergo thermomechanical treatments that promote a sound microstructure free of defects generated in AM metallic materials.

5. Conclusions

This study investigated the fatigue behaviour and damage mechanisms of cyclically strained 316L stainless steel additively manufactured using L-PBF. High-cycle fatigue regime tests were conducted on two steels: as-built and heat-treated at 900 °C. This study provides fundamental insights into the fatigue damage mechanisms of metallic materials additively manufactured using L-PBF. The following conclusions can be drawn.

1. A significant improvement in the fatigue strength of as-built AM 316L was observed after heat treatment. The fatigue limit of AM 316L increased from 75 to 150 MPa with the proposed heat treatment at 900 °C.
2. The LPBF-induced microstructural characteristics, that is, pores, dendritic cellular structure, and residual stresses, are the main causes of fatigue damage in the as-built 316L. With heat treatment at 900 °C, the causes of fatigue damage in the HT 316L were significantly reduced because residual stress and cellular structure were significantly reduced.
3. Intensive persistent slip bands (PSBs) were promoted during the cyclic straining of HT 316L. Subsequently, these localised strain bands intersect with the surface boundaries, generating crack embryos at these boundaries.
4. Based on the microindentation hardness measurements before and after cyclic plastic deformation, a cyclic hardening ratio of ~18% was observed for HT 316L. In contrast, a distinct cyclic softening of 22% is promoted in the counterparts of AB 316L.
5. The AM 316L materials under the studied conditions, AB and HT, exhibited a significantly low ratio of fatigue limit/tensile strength, σ_{FL}/σ_{UTS} 0.12–0.24, which is inconsistent with that commonly reported for wrought steels of 0.4–0.6. Thus, the prevalent ratio of σ_{FL}/σ_{UTS} could not be applied to the AM 316L.
6. Further investigations can be conducted from this knowledge concerning the fatigue damage mechanism in the as-built structure and that in the heat-treated structures at different temperatures to increase their significance and achieve the highest fatigue resistance.

CRediT authorship contribution statement

Atef Hamada: Conceptualization, Visualization, Formal analysis, Investigation, Methodology, Writing - original draft, Writing - review & editing. **Matias Jaskari:** Methodology, Conducting fatigue experiments. **Tejas Gundgire:** Methodology, Conducting residual stress measurements. **Antti Järvenpää:** Funding acquisition.

Declaration of competing interest

The authors declare that they have no known competing financial interests or personal relationships that could have appeared to influence the work reported in this paper.

Data availability

No data was used for the research described in the article.

References

[1] A. Seharing, A.H. Azman, S. Abdullah, Systematic review: overview on trends and future opportunities of additive manufactured lattice structures, Struct. Integr. 23 (2022) 75–90, https://doi.org/10.1007/978-3-030-85646-5_6.
[2] H.M. Hamza, K.M. Deen, A. Khaliq, E. Asselin, W. Haider, Microstructural, corrosion and mechanical properties of additively manufactured alloys: a review, Crit. Rev. Solid State Mater. Sci. 47 (2022) 46–98, https://doi.org/10.1080/10408436.2021.1886044.
[3] A. du Plessis, S.M.J. Razavi, M. Benedetti, S. Murchio, M. Leary, M. Watson, D. Bhate, F. Berto, Properties and applications of additively manufactured metallic cellular materials: a review, Prog. Mater. Sci. 125 (2022), 100918, https://doi.org/10.1016/J.PMATSCI.2021.100918.
[4] T. Ronneberg, C.M. Davies, P.A. Hooper, Revealing relationships between porosity, microstructure and mechanical properties of laser powder bed fusion 316L

stainless steel through heat treatment, Mater. Des. 189 (2020), https://doi.org/10.1016/J.MATDES.2020.108481.

[5] A. Charmi, R. Falkenberg, L. Ávila, G. Mohr, K. Sommer, A. Ulbricht, M. Sprengel, R. Saliwan Neumann, B. Skrotzki, A. Evans, Mechanical anisotropy of additively manufactured stainless steel 316L: an experimental and numerical study, Mater. Sci. Eng. A. 799 (2021), https://doi.org/10.1016/J.MSEA.2020.140154.

[6] A. Yadollahi, N. Shamsaei, Additive manufacturing of fatigue resistant materials: challenges and opportunities, Int. J. Fatig. 98 (2017) 14–31, https://doi.org/10.1016/J.IJFATIGUE.2017.01.001.

[7] H.R. Kotadia, G. Gibbons, A. Das, P.D. Howes, A review of laser powder bed fusion additive manufacturing of aluminium alloys: microstructure and properties, Addit. Manuf. 46 (2021), 102155, https://doi.org/10.1016/j.addma.2021.102155.

[8] M. Benedetti, C. Santus, Notch fatigue and crack growth resistance of Ti-6Al-4V ELI additively manufactured via selective laser melting: a critical distance approach to defect sensitivity, Int. J. Fatig. 121 (2018) 281–292, https://doi.org/10.1016/j.ijfatigue.2018.12.020.

[9] K. Gruber, P. Szymczyk-Ziółkowska, S. Dziuba, S. Duda, P. Zielonka, S. Seitl, G. Lesiuk, Fatigue crack growth characterization of Inconel 718 after additive manufacturing by laser powder bed fusion and heat treatment, Int. J. Fatig. 166 (2023), https://doi.org/10.1016/J.IJFATIGUE.2022.107287.

[10] S.F. Siddiqui, E. Araiza, Microstructural defects governing torsional fatigue failure of additively manufactured as-built and heat-treated Inconel 718, Eng. Fail. Anal. 144 (2023), 106975, https://doi.org/10.1016/j.engfailanal.2022.106975.

[11] G. Meneghetti, D. Rigon, C. Gennari, An analysis of defects influence on axial fatigue strength of maraging steel specimens produced by additive manufacturing, Int. J. Fatig. 118 (2019) 54–64, https://doi.org/10.1016/j.ijfatigue.2018.08.034.

[12] C. Douellou, X. Balandraud, E. Duc, B. Verquin, F. Lefebvre, F. Sar, Rapid characterization of the fatigue limit of additive-manufactured maraging steels using infrared measurements, Addit. Manuf. 35 (2020), https://doi.org/10.1016/j.addma.2020.101310.

[13] C. Elangeswaran, A. Cutolo, G.K. Muralidharan, K. Vanmeensel, B. Van Hooreweder, Microstructural analysis and fatigue crack initiation modelling of additively manufactured 316L after different heat treatments, Mater. Des. 194 (2020), https://doi.org/10.1016/j.matdes.2020.108962.

[14] Y. Wang, Z. Su, Effect of micro-defects on fatigue lifetime of additive manufactured 316L stainless steel under multiaxial loading, Theor. Appl. Fract. Mech. 111 (2021), 102849, https://doi.org/10.1016/j.tafmec.2020.102849.

[15] W. Abd-Elaziem, S. Elkatatny, A.-E. Abd-Elaziem, M. Khedr, M.A. Abd El-baky, M. A. Hassan, M. Abu-Okail, M. Mohammed, A. Järvenpää, T. Allam, A. Hamada, On the current research progress of metallic materials fabricated by laser powder bed fusion process: a review, J. Mater. Res. Technol. 20 (2022) 681–707, https://doi.org/10.1016/J.JMRT.2022.07.085.

[16] K.H. Lo, C.H. Shek, J.K.L. Lai, Recent developments in stainless steels, Mater. Sci. Eng. R Rep. 65 (2009) 39–104, https://doi.org/10.1016/J.MSER.2009.03.001.

[17] N. Ahmed, I. Barsoum, G. Haidemenopoulos, R.K.A. Al-Rub, Process parameter selection and optimization of laser powder bed fusion for 316L stainless steel: a review, J. Manuf. Process. 75 (2022) 415–434, https://doi.org/10.1016/j.jmapro.2021.12.064.

[18] M. Jaskari, S. Ghosh, I. Miettunen, P. Karjalainen, A. Järvenpää, Tensile properties and deformation of AISI 316L additively manufactured with various energy densities, Mater 14 (2021) 5809, https://doi.org/10.3390/MA14195809, 14 (2021) 5809.

[19] C. Sánchez De, R. Candela, A. Riquelme, P. Rodrigo, B. Torres, J. Rams, Wear behavior of additively manufactured 316L/SiCp composites with up to 60 wt% SiCp, Ceram. Int. 48 (2022) 33736–33750, https://doi.org/10.1016/j.ceramint.2022.07.319.

[20] L. Zhang, W. Zhai, W. Zhou, X. Chen, L. Chen, B. Han, L. Cao, G. Bi, Improvement of mechanical properties through inhibition of oxidation by adding TiC particles in laser aided additive manufacturing of stainless steel 316L, Mater. Sci. Eng. A. 853 (2022), https://doi.org/10.1016/j.msea.2022.143767.

[21] W. Zhai, W. Zhou, S.M.L. Nai, In-situ formation of TiC nanoparticles in selective laser melting of 316L with addition of micronsized TiC particles, Mater. Sci. Eng. A. 829 (2022), https://doi.org/10.1016/J.MSEA.2021.142179.

[22] W. Zhai, W. Zhou, S.M.L. Nai, Grain refinement and strengthening of 316L stainless steel through addition of TiC nanoparticles and selective laser melting, Mater. Sci. Eng. A. 832 (2022), https://doi.org/10.1016/J.MSEA.2021.142460.

[23] W. Zhai, Z. Zhu, W. Zhou, S.M.L. Nai, J. Wei, Selective laser melting of dispersed TiC particles strengthened 316L stainless steel, Compos. B Eng. 199 (2020), https://doi.org/10.1016/J.COMPOSITESB.2020.108291.

[24] T.H. Becker, P. Kumar, U. Ramamurty, Fracture and fatigue in additively manufactured metals, Acta Mater. 219 (2021), 117240, https://doi.org/10.1016/J.ACTAMAT.2021.117240.

[25] H. Roirand, B. Malard, A. Hor, N. Saintier, Effect of laser scan pattern in laser powder bed fusion process: the case of 316L stainless steel, Procedia Struct. Integr. 38 (2022) 149–158, https://doi.org/10.1016/J.PROSTR.2022.03.016.

[26] M. Pelegatti, D. Benasciutti, F. De Bona, A. Lanzutti, M. Magnan, J. Srnec Novak, E. Salvati, F. Sordetti, M. Sortino, G. Totis, E. Vaglio, On the factors influencing the elastoplastic cyclic response and low cycle fatigue failure of AISI 316L steel produced by laser-powder bed fusion, Int. J. Fatig. 165 (2022), 107224, https://doi.org/10.1016/j.ijfatigue.2022.107224.

[27] J. Kluczyński, L. Śnieżek, K. Grzelak, J. Torzewski, I. Szachogłuchowicz, M. Wachowski, The influence of process parameters on the low-cycle fatigue properties of 316L steel parts produced by powder bed fusion, Metall. Mater. Trans. A Phys. Metall. Mater. Sci. 54 (2022) 196–210, https://doi.org/10.1007/S11661-022-06858-0/FIGURES/13.

[28] X. Liang, A. Hor, C. Robert, M. Salem, F. Lin, F. Morel, High cycle fatigue behavior of 316L steel fabricated by laser powder bed fusion: effects of surface defect and loading mode, Int. J. Fatig. 160 (2022), 106843, https://doi.org/10.1016/j.ijfatigue.2022.106843.

[29] S. Hatami, T. Ma, T. Vuoristo, J. Bertilsson, O. Lyckfeldt, Fatigue Strength of 316 L Stainless Steel Manufactured by Selective Laser Melting, J. Mater. Eng. Perform. 29 (n.d.) 3183–3194. https://doi.org/10.1007/s11665-020-04859-x.

[30] J.W. Pegues, M.D. Roach, N. Shamsaei, Additive Manufacturing of Fatigue Resistant Austenitic Stainless Steels by Understanding Process-Structure-Property Relationships, vol. 8, 2020, pp. 8–15, https://doi.org/10.1080/21663831.2019.1678202.

[31] T. Rautio, M. Jaskari, T. Gundgire, T. Iso-Junno, M. Vippola, A. Järvenpää, The effect of severe shot peening on fatigue life of laser powder bed fusion manufactured 316L stainless steel, Mater 15 (2022) 3517, https://doi.org/10.3390/MA15103517, 15 (2022) 3517.

[32] A. Malakizadi, D. Mallipeddi, S. Dadbakhsh, R. M'saoubi, P. Krajnik, Post-processing of additively manufactured metallic alloys-A review keywords: additive manufacturing powder bed fusion direct energy deposition machining grinding mechanical properties machinability grindability laser polishing finishing electropolishing fatigue wear corrosion 316L Ti6Al4V alloy 718, Int. J. Mach. Tool Manufact. 179 (2022), 103908, https://doi.org/10.1016/j.ijmachtools.2022.103908.

[33] T. Rautio, H. Torbati-Sarraf, T. Allam, A. Järvenpää, A. Hamada, Enhancement of electrical conductivity and corrosion resistance by gold-nickel coating of additively manufactured AlSi10Mg alloy, J. Mater. Res. Technol. 17 (2022) 521–536, https://doi.org/10.1016/J.JMRT.2022.01.022.

[34] F. Fan, M. Jiang, P. Wang, C. Liu, Z. Liu, Z. Chen, Defect-associated microstructure evolution and deformation heterogeneities in additively manufactured 316L stainless steel, Mater. Sci. Eng. A. 861 (2022), https://doi.org/10.1016/j.msea.2022.144287.

[35] A.K. Agrawal, D.J. Thoma, High-throughput surface characterization to identify porosity defects in additively manufactured 316L stainless steel, Addit. Manuf. Lett. 3 (2022), 100093, https://doi.org/10.1016/J.ADDLET.2022.100093.

[36] T. Rautio, A. Hamada, J. Kumpula, A. Järvenpää, T. Allam, Enhancement of electrical conductivity and corrosion resistance by silver shell-copper core coating of additively manufactured AlSi10Mg alloy, Surf. Coating. Technol. 403 (2020), 126426, https://doi.org/10.1016/J.SURFCOAT.2020.126426.

[37] L. An, D. Wang, D. Zhu, Improvement on surface quality of 316L stainless steel fabricated by laser powder bed fusion via electrochemical polishing in NaNO3 solution, J. Manuf. Process. 83 (2022) 325–338, https://doi.org/10.1016/J.JMAPRO.2022.09.005.

[38] F. Yan, W. Xiong, E. Faierson, G.B. Olson, Characterization of nano-scale oxides in austenitic stainless steel processed by powder bed fusion, Scripta Mater. 155 (2018) 104–108, https://doi.org/10.1016/J.SCRIPTAMAT.2018.06.011.

[39] L. Yao, S. Huang, U. Ramamurty, Z. Xiao, On the formation of "Fish-scale" morphology with curved grain interfacial microstructures during selective laser melting of dissimilar alloys, Acta Mater. 220 (2021), 117331, https://doi.org/10.1016/J.ACTAMAT.2021.117331.

[40] Y. Zhong, L. Liu, S. Wikman, D. Cui, Z. Shen, Intragranular cellular segregation network structure strengthening 316L stainless steel prepared by selective laser melting, J. Nucl. Mater. 470 (2016) 170–178, https://doi.org/10.1016/J.JNUCMAT.2015.12.034.

[41] C. Qiu, M. Al Kindi, A.S. Aladawi, I. Al Hatmi, A comprehensive study on microstructure and tensile behaviour of a selectively laser melted stainless steel, Sci. Rep. 81 (8) (2018) 1–16, https://doi.org/10.1038/s41598-018-26136-7, 2018.

[42] E. Edin, F. Svahn, P. Åkerfeldt, M. Eriksson, M.-L. Antti, Rapid method for comparative studies on stress relief heat treatment of additively manufactured 316L, Mater. Sci. Eng. A. 847 (2022), 143313, https://doi.org/10.1016/J.MSEA.2022.143313.

[43] Z. Sun, X. Tan, S.B. Tor, W.Y. Yeong, Selective laser melting of stainless steel 316L with low porosity and high build rates, Mater. Des. 104 (2016) 197–204, https://doi.org/10.1016/J.MATDES.2016.05.035.

[44] C. Zhao, Y. Bai, Y. Zhang, X. Wang, J.M. Xue, H. Wang, Influence of scanning strategy and building direction on microstructure and corrosion behaviour of selective laser melted 316L stainless steel, Mater. Des. 209 (2021), https://doi.org/10.1016/J.MATDES.2021.109999.

[45] Y.J. Yin, J.Q. Sun, J. Guo, X.F. Kan, D.C. Yang, Mechanism of high yield strength and yield ratio of 316 L stainless steel by additive manufacturing, Mater. Sci. Eng. A. 744 (2019) 773–777, https://doi.org/10.1016/J.MSEA.2018.12.092.

[46] J. Nafar Dastgerdi, O. Jaberi, H. Remes, Influence of internal and surface defects on the fatigue performance of additively manufactured stainless steel 316L, Int. J. Fatig. 163 (2022), 107025, https://doi.org/10.1016/J.IJFATIGUE.2022.107025.

[47] Z. Wang, S. Yang, Y. Huang, C. Fan, Z. Peng, Z. Gao, R. Pippan, Microstructure and fatigue damage of 316L stainless steel manufactured by selective laser melting (SLM), Materials 14 (2021) 7544, https://doi.org/10.3390/ma14247544.

[48] G.S. Ponticelli, R. Panciroli, S. Venettacci, F. Tagliaferri, S. Guarino, Experimental investigation on the fatigue behavior of laser powder bed fused 316L stainless steel, CIRP J. Manuf. Sci. Technol. 38 (2022) 787–800, https://doi.org/10.1016/J.CIRPJ.2022.07.007.

[49] M. Zhang, C.N. Sun, X. Zhang, P.C. Goh, J. Wei, D. Hardacre, H. Li, Fatigue and fracture behaviour of laser powder bed fusion stainless steel 316L: influence of processing parameters, Mater. Sci. Eng. A. 703 (2017) 251–261, https://doi.org/10.1016/J.MSEA.2017.07.071.

[50] F. Zeng, Y. Yang, G. Qian, Fatigue properties and S-N curve estimating of 316L stainless steel prepared by SLM, Int. J. Fatig. 162 (2022), 106946, https://doi.org/10.1016/J.IJFATIGUE.2022.106946.

[51] R. Shrestha, J. Simsiriwong, N. Shamsaei, Fatigue behavior of additive manufactured 316L stainless steel parts: effects of layer orientation and surface roughness, Addit. Manuf. 28 (2019) 23–38, https://doi.org/10.1016/J.ADDMA.2019.04.011.

[52] B. Blinn, F. Krebs, M. Ley, R. Teutsch, T. Beck, Determination of the influence of a stress-relief heat treatment and additively manufactured surface on the fatigue behavior of selectively laser melted AISI 316L by using efficient short-time procedures, Int. J. Fatig. 131 (2020), 105301, https://doi.org/10.1016/J.IJFATIGUE.2019.105301.

[53] O. Andreau, E. Pessard, I. Koutiri, P. Peyre, N. Saintier, Influence of the position and size of various deterministic defects on the high cycle fatigue resistance of a 316L steel manufactured by laser powder bed fusion, Int. J. Fatig. 143 (2021), 105930, https://doi.org/10.1016/J.IJFATIGUE.2020.105930.

[54] O. Andreau, E. Pessard, I. Koutiri, J.D. Penot, C. Dupuy, N. Saintier, P. Peyre, A competition between the contour and hatching zones on the high cycle fatigue behaviour of a 316L stainless steel: analyzed using X-ray computed tomography, Mater. Sci. Eng. A 757 (2019) 146–159, https://doi.org/10.1016/J.MSEA.2019.04.101.

[55] T. Tomaszewski, Modelling of critical defect distributions for estimating the size effect of selective laser melted 316L stainless steel, Int. J. Fatig. 167 (2023), 107378, https://doi.org/10.1016/J.IJFATIGUE.2022.107378.

[56] A.S. Hamada, A. Järvenpää, M.M.Z. Ahmed, M. Jaskari, B.P. Wynne, D.A. Porter, L.P. Karjalainen, The microstructural evolution of friction stir welded AA6082-T6 aluminum alloy during cyclic deformation, Mater. Sci. Eng. A 642 (2015) 366–376, https://doi.org/10.1016/J.MSEA.2015.06.100.

[57] S. Lee, J.W. Pegues, N. Shamsaei, Fatigue behavior and modeling for additive manufactured 304L stainless steel: the effect of surface roughness, Int. J. Fatig. 141 (2020), 105856, https://doi.org/10.1016/J.IJFATIGUE.2020.105856.

[58] Y. Wang, X. Zhang, Z. Su, W. Yao, Multiaxial fatigue life prediction based on single defect for additively manufactured 316L, Int. J. Fatig. 163 (2022), 107101, https://doi.org/10.1016/J.IJFATIGUE.2022.107101.

[59] P.D. Nezhadfar, R. Shrestha, N. Phan, N. Shamsaei, Fatigue behavior of additively manufactured 17-4 PH stainless steel: synergistic effects of surface roughness and heat treatment, Int. J. Fatig. 124 (2019) 188–204, https://doi.org/10.1016/J.IJFATIGUE.2019.02.039.

[60] J. Gockel, L. Sheridan, B. Koerper, B. Whip, The influence of additive manufacturing processing parameters on surface roughness and fatigue life, Int. J. Fatig. 124 (2019) 380–388, https://doi.org/10.1016/J.IJFATIGUE.2019.03.025.

[61] K. Solberg, S. Guan, S.M.J. Razavi, T. Welo, K.C. Chan, F. Berto, Fatigue of additively manufactured 316L stainless steel: the influence of porosity and surface roughness, Fatig. Fract. Eng. Mater. Struct. 42 (2019) 2043–2052, https://doi.org/10.1111/FFE.13077.

[62] A.S. Hamada, L.P. Karjalainen, J. Puustinen, Fatigue behavior of high-Mn TWIP steels, Mater. Sci. Eng. A 517 (2009) 68–77, https://doi.org/10.1016/J.MSEA.2009.03.039.

[63] A. Hamada, D. Porter, J. Puustinen, L. Pentti Karjalainen, Study on cyclic strain localization and fatigue fracture mechanism in high manganese twinning-induced plasticity steels, Mater. Sci. Forum 762 (2013) 411–417, https://doi.org/10.4028/WWW.SCIENTIFIC.NET/MSF.762.411.

[64] J. Schijve, Fatigue of Structures and Materials, second ed., Springer, Dordrecht, Germany, 2004 https://doi.org/10.1007/0-306-48396-3.

[65] A. Riemer, S. Leuders, M. Thöne, H.A. Richard, T. Tröster, T. Niendorf, On the fatigue crack growth behavior in 316L stainless steel manufactured by selective laser melting, Eng. Fract. Mech. 120 (2014) 15–25, https://doi.org/10.1016/J.ENGFRACMECH.2014.03.008.

[66] J. Man, K. Obrtlík, J. Polák, Extrusions and intrusions in fatigued metals. Part 1. State of the art and history, Philos. Mag. 89 (2009) 1295–1336, https://doi.org/10.1080/14786430902917616.

[67] F. Bayerlein, F. Bodensteiner, C. Zeller, M. Hofmann, M.F. Zaeh, Transient development of residual stresses in laser beam melting – a neutron diffraction study, Addit. Manuf. 24 (2018) 587–594, https://doi.org/10.1016/J.ADDMA.2018.10.024.

[68] A.S. Wu, D.W. Brown, M. Kumar, G.F. Gallegos, W.E. King, An experimental investigation into additive manufacturing-induced residual stresses in 316L stainless steel, Metall. Mater. Trans. A Phys. Metall. Mater. Sci. 45 (2014) 6260–6270, https://doi.org/10.1007/S11661-014-2549-X/FIGURES/11.

[69] P. Bian, J. Shi, Y. Liu, Y. Xie, Influence of laser power and scanning strategy on residual stress distribution in additively manufactured 316L steel, Opt Laser. Technol. 132 (2020), 106477, https://doi.org/10.1016/J.OPTLASTEC.2020.106477.

[70] M. Shiomi, K. Osakada, K. Nakamura, T. Yamashita, F. Abe, Residual stress within metallic model made by selective laser melting process, CIRP Ann 53 (2004) 195–198, https://doi.org/10.1016/S0007-8506(07)60677-5.

[71] M.D. Chapetti, H. Miyata, T. Tagawa, T. Miyata, M. Fujioka, Fatigue strength of ultra-fine grained steels, Mater. Sci. Eng. A 381 (2004) 331–336, https://doi.org/10.1016/J.MSEA.2004.04.055.

[72] A.S. Hamada, Deformation and damage mechanisms in ultrafine-grained austenitic stainless steel during cyclic straining, Metall. Mater. Trans. A Phys. Metall. Mater. Sci. 44 (2013) 1626–1630, https://doi.org/10.1007/s11661-012-1578-6.